



Mechanical properties of 3D printed polymeric cellular materials with triply periodic minimal surface architectures



Diab W. Abueidda^{a,*}, Mete Bakir^a, Rashid K. Abu Al-Rub^b, Jörgen S. Bergström^c, Nahil A. Sobh^{a,d}, Iwona Jasiuk^{a,*}

^a Department of Mechanical Science and Engineering, University of Illinois at Urbana-Champaign, 1206 West Green Street, Urbana, IL 61801-2906, USA

^b Institute Center for Energy, Mechanical and Materials Engineering Department, Masdar Institute of Science and Technology, Abu Dhabi, UAE

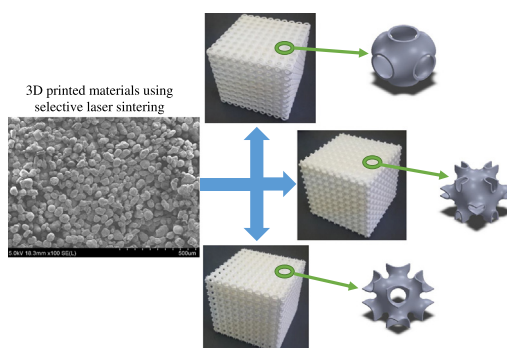
^c Veryst Engineering, 47A Kearney Road, Needham, MA 02494, USA

^d Beckman Institute for Advanced Science and Technology, University of Illinois at Urbana-Champaign, 405 N Mathews Ave, Urbana, IL 61801, USA

HIGHLIGHTS

- Triply periodic minimal surfaces (TPMS) are utilized to create new cellular materials (CMs).
- The modulus and strength of three types of TPMS-CMs are found experimentally and computationally.
- Post-yielding behavior of the three TPMS-CMs is reported and discussed.
- Failure (buckling vs. yielding) maps are reported.

GRAPHICAL ABSTRACT



ARTICLE INFO

Article history:

Received 27 December 2016

Received in revised form 5 March 2017

Accepted 6 March 2017

Available online 08 March 2017

Keywords:

Architected materials

3D printing

Mechanical testing

Polymeric cellular materials

Finite element analysis

ABSTRACT

In this paper, three types of triply periodic minimal surfaces (TPMS) are utilized to create novel polymeric cellular materials (CM). The TPMS architectures considered are Schwarz Primitive, Schoen IWP, and Neovius. This work investigates experimentally and computationally mechanical properties of these three TPMS-CMs. 3D printing is used to fabricate these polymeric cellular materials and their base material. Their properties are tested to provide inputs and serve as validation for finite element modeling. Two finite deformation elastic/hyperelastic-viscoplastic constitutive models calibrated based on the mechanical response of the base material are used in the computational study of the TPMS-CMs. It is shown that the specimen size of the TPMS-CMs affect their mechanical properties. Moreover, the finite element results agree with the results obtained experimentally. The Neovius-CM and IWP-CM have a similar mechanical response, and it is found that they have higher stiffness and strength than the Primitive-CM.

© 2017 Elsevier Ltd. All rights reserved.

1. Introduction

Discovery of new lightweight yet strong materials is of high scientific and technological interest as they can be utilized in numerous engineering applications (e.g. automotive and aerospace industry) [1–4]. Researchers investigated the effects of base materials, density, and

* Corresponding authors.

E-mail addresses: diababueidda@gmail.com (D.W. Abueidda), ijasiuk@illinois.edu (I. Jasiuk).

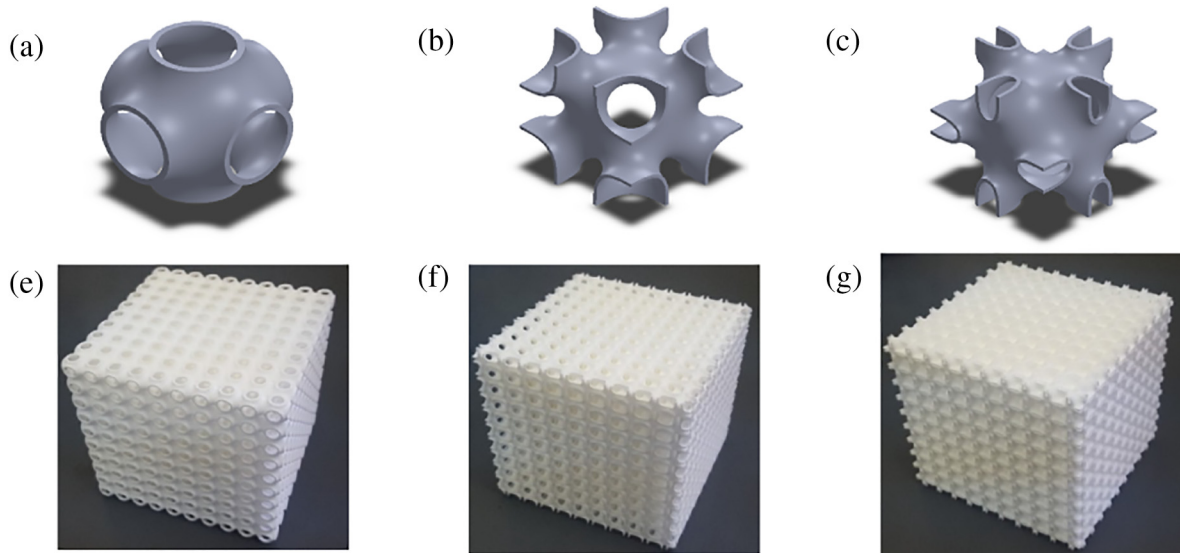


Fig. 1. CAD drawings of TPMS-CMs with a relative density of 10%: (a) Primitive-CM, (b) IWP-CM, (c) Neovius-CM. 3D printed specimens: (e) Primitive-CM (relative density is 23.5%), (f) IWP-CM (relative density is 25.6%), (g) Neovius-CM (relative density is 23.7%).

foam's architecture on the overall performance of cellular materials. The geometry of architected materials can be designed, based on engineering optimization process, or inspired. In architected materials, the morphology of their structures yields properties that are not available in bulk, continuous media. Moreover, researchers have designed and created materials with architectures that are inspired by nature. Natural and biological materials possess characteristics such as hierarchical, optimized periodic and multifunctional structuring, size effect strengthening, and high interconnectivity [2,5–8].

Furthermore, the architectures of cellular materials control the way the materials get deformed: in a bending-dominated mode or a stretching-dominated mode [9]. Structures that are statically and kinematically determinate are stretching-dominated and support external loads by only compressive and tensile loadings [10,11]. Therefore, materials deforming in a stretching-dominated mode have higher stiffness and strength than the ones deforming in a bending-dominated mode. Cellular materials with stochastic porosity usually deform through bending of walls and trusses [12]. Also, stochastic structuring usually introduces imperfections which reduce the overall mechanical properties. Thus, periodic structures are more desirable than the stochastic ones [5,7,13]. Several researchers have used experimental, computational, and analytical approaches to study linear and nonlinear mechanical responses of cellular materials including elastic

properties, yielding, buckling, and effects of imperfections [1,14,15]. They showed that the wall thickness (or relative density) of the cellular materials governs the failure mechanisms and that imperfections in cellular materials such as octet-truss might lead to dramatic deterioration in strength. In addition to the effect of the architecture of the microstructure and relative density of the cellular materials, the mechanical behavior of cellular materials is directly affected by the scale at which they are made and base materials they are fabricated from [16]. The architecture of cellular materials can be designed and optimized to create materials with multifunctional properties including high stiffness, strength, energy absorption, and damage-tolerance, among others [4,7,17]. One of the most common cellular materials is a honeycomb which is anisotropic material. One of the main reasons that honeycomb structures are attractive is that their microstructures allow large deformations which in turn lead to high specific energy dissipation capacity [18]. Restrepo et al. [19] fabricated periodic cellular materials (two types of honeycombs) using a shape memory polymer as a base material. They introduced a new class of programmable materials whose mechanical performance is modified after manufacturing. Further, cellular materials can be used to create materials with unconventional properties such as negative Poisson's ratio [18,20–23]. Bertoldi et al. [24] utilized elastic instabilities of periodic cellular materials to create 2D materials with negative Poisson's

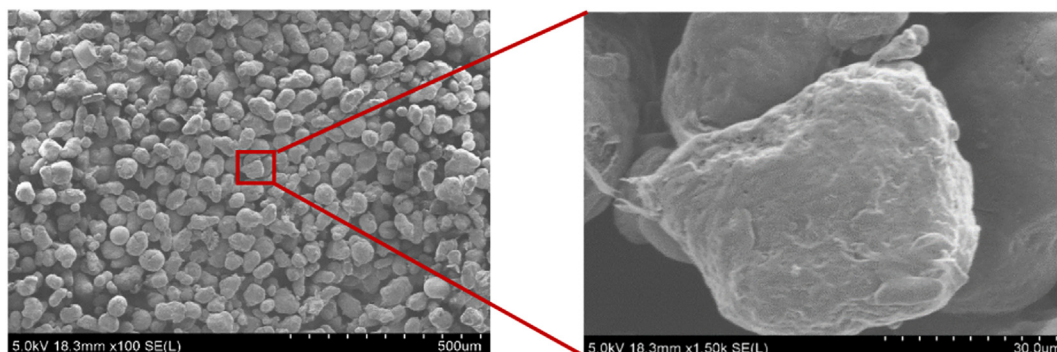


Fig. 2. SEM images of PA 2200 fabricated using the 3D printer Formiga 100.

ratio under compressive loads. Additionally, Iio et al. [25] established finite element model to study the elastoplastic compressive deformation of hollow-strut cellular materials. A linear response is observed in the elastic region, and it is followed by yielding and stress plateau. After that, a gradual increase in the plastic flow stress is noticed.

Polymeric cellular materials can be fabricated through polymer foaming processes [26], wherein either physical blowing agents [27] or chemical blowing agents [28,29] are utilized to generate cellular materials. Such processes give rise to random structures. 3D printing is another technique to fabricate polymeric cellular materials. Advances in 3D printing have allowed the fabrication of various types of cellular materials with dimensions ranging from the submicron to the centimeter level, and the investigation of the mechanical response of such cellular materials [30,31]. 3D printing offers outstanding control over the architectures and base materials of cellular structures and allows the fabrication of structures with complicated architectures using various materials [30,32].

Examples of architected materials are the mathematically well-known triply periodic minimal surfaces (TPMS) [33]. TPMS are promising porous structures which can be used to create multifunctional materials for various technological applications. TPMS are infinitely extending, smooth, and continuous surfaces that divide the space into two congruent intertwined regions. Each region has a volume fraction of 50% and is periodic in 3D [34,35]. Additionally, the summation of the principal curvatures at each point on the TPMS is zero, i.e., TPMS possess a zero mean curvature [36,37]. Recently, researchers have studied thermal and electrical conductivities, the coefficient of thermal expansion, and elastic properties of structures inspired by TPMS. The TPMS have been used to create interpenetrating phase composites (IPCs) in which each phase is interconnected and continuous in 3D [5, 38–43]. Abueidda et al. [40–42] have concluded that TPMS-IPCs have superior and robust properties compared to other types of composite materials due to the continuity and interconnectivity of the phases of TPMS-IPCs. Wang et al. [43] investigated the elastic properties, strength, and energy dissipation of bi-continuous composites based on three different TPMS-like geometries. Moreover, TPMS have been used to generate novel cellular materials (CMs) with different relative densities (the ratio between the density of the TPMS-CMs and the density of the solid base) [32,34,44]. Abueidda et al. [32] studied the electrical/thermal

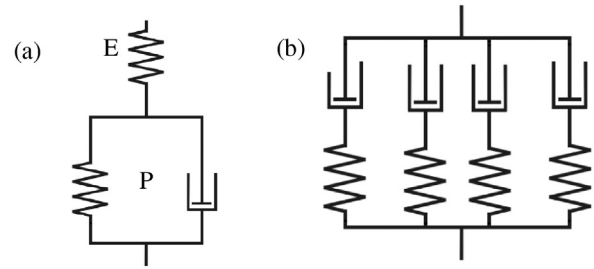


Fig. 3. Rheological representation of the constitutive models; (a) AB model (b) FEN model.

conductivities, elastic moduli (uniaxial modulus, shear modulus, and bulk modulus), and anisotropy of the conductivity and elasticity tensors of six different types of TPMS-CMs. The analyses of TPMS-CMs were performed using a finite element method with periodic boundary conditions applied to the unit cells of TPMS-CMs. Furthermore, Han et al. [44] used Primitive structure to fabricate cellular materials with properties (stiffness and strength) better than those of lattices. The Primitive-CM considered in [44] are modified so the size of the openings is smaller and the geometry is elongated in the vertical direction. For such architecture, the performance is enhanced in the vertical direction while it deteriorates in the other directions.

One advantage of using TPMS structures to create cellular materials is to overcome the common weaknesses of truss/strut-based structures. The truss/strut structures induce stress concentrations and are likely to have imperfections around the connections between the truss elements which in turn cause the structure to collapse at lower applied loads [10, 32]. For example, Khaderi et al. [9] concluded that imperfections in the Gyroid-lattice cause a severe knock-down in its elastic and plastic properties. Joints and struts do not exist in the TPMS-CMs. The connectivity and continuity of the TPMS-CMs allow a smoother transfer of loads (see Fig. 1) [32] which leads to a better integrity of the TPMS-CMs compared to truss/strut-based CMs possessing joints.

In this paper, three types of TPMS-CMs are fabricated using 3D printing, and then their linear and nonlinear mechanical responses are investigated experimentally and computationally. Their mechanical behaviors are studied using a finite element method under periodic and mixed boundary conditions. The mechanical properties of the polymeric TPMS-CMs considered in the current work include the elastic stiffness, buckling, yielding, post-yielding, and dissipation energy. Buckling analysis is performed to address potential instability failure of the TPMS-CMs due to geometric effects. Even though local buckling will not lead to an immediate loss of material resistance, local buckling may lead to dramatic decrease in the ability of buckled unit cells to constrain adjacent cells against translation and rotation [45]. Imperfections in the structures, which are unavoidable in many cases, and eccentric loads influence the stability behavior regarding the critical load values and deformation characteristics. Two constitutive relations, namely Arruda-Boyce (AB) model [46,47] and flow evolution network (FEN) model [48], are adopted to capture the behavior of TPMS-CMs and the base polymer used to fabricate the TPMS-CMs.

2. Experimental procedure

2.1. Material fabrication

3D printing based on selective laser sintering technology was employed in fabricating the TPMS-CMs. Specifically, the 3D printer “Formiga P100” and a commercial material called “PA 2200,” and based on polyamide 12, were utilized to fabricate the polymeric TPMS-CM specimens and the specimens of the base material used for calibration [49–51]. The 3D printer “Formiga P100” has a layer thickness

Table 1

Statistical study for the experimental results of the TPMS-CMs. SD, RD, E, and S represent the standard deviation, relative density, modulus, and strength, respectively. The subscript M stands for the mean of the variable.

RD (%)	(SD _{RD} /RD _M) (%)	(SD _E /E _M) (%)	(SD _S /S _M) (%)
Primitive-CM			
4.8%	1.9	7.25	3.15
5.4%	2.27	8.87	11.06
6.6%	5.67	4.68	5.5
12.6%	3.17	0.2	5.27
16.4%	1.04	2.72	1.88
23.5%	1.14	4.19	0.96
Neovius-CM			
9.8%	1.89	8.85	7.15
10.4%	2.42	1.91	2.64
15.2%	4.48	5.17	4.67
16.0%	4.36	3.59	9.71
23.7%	4.2	5.3	8.16
IWP-CM			
8.1%	6.15	10.44	11.78
9.1%	4.8	7.72	9.99
10.6%	3.93	3.35	5.01
14.0%	3.37	3.66	4.66
20.9%	3.65	4.38	4.79
25.6%	5.31	1.84	4.27

of 0.1 mm and a laser power of 30 W. The specimens were 3D printed at an operational temperature of 172.5 °C. Fig. 2 shows scanning electron microscopy (SEM) images of the 3D printed PA 2200. Fig. 2 illustrates the sintered powdered polymer and portrays that the diameter of a particle is approximately 45 μm . The size of the particles significantly affects the properties of the material and controls the dimensions of the printed specimens. Moreover, the 3D printing technology induces anisotropic behavior due to the layer-wise fabrication process [50]. Therefore, it is expected to have anisotropy in the mechanical properties of the 3D printed TPMS-CMs.

2.2. Mechanical testing

The mechanical behavior of polymers is strongly dependent on the applied strain rate, material type, and temperature. Although temperature has utmost effect on the mechanical properties of polymers, its effect is neglected by performing all the mechanical tests at room temperature. To obtain the mechanical response of the base material, the ASTM D638-10 Type I standard was used for uniaxial tension whereas for the uniaxial compression the ASTM D695-15 standard was used. The base material and TPMS-CMs were tested under displacement control using Instron 4400 with a load cell of 30 kN or 100 kN depending on the required loads. Tensile and compressive loadings were used for the base material while only compressive loading was applied on the TPMS-CMs. Moreover, all specimens were tested one week after their fabrication to eliminate possible changes in the mechanical

properties of the polymer due to ageing or degradation effects. Cooke et al. [52] studied the effect of storing the materials fabricated using selective laser sintering on the mechanical properties. They reported that the modulus and strength were significantly reduced due to moisture absorption after storing the 3D printed materials in a non-desiccated environment. During the test, the specimens were positioned in the center of the loading frame to ensure uniform loading and to eliminate moments induced by specimen misalignments. Also, for compression testing, aluminum plates with a lubricating fluid on their surfaces were placed on the top and bottom of the specimens to reduce friction which causes a state of nonhomogeneous deformation, usually called as barrelling of the test specimen. The base material was tested to characterize its mechanical response and to use the obtained stress-strain curves to calibrate the constitutive models adopted in computations. In the case of tensile loading, some of the specimens were tested under loading and unloading, and some of the specimens were tested until failure in both printing directions (horizontal and vertical directions). In the case of compression loading, the specimens were tested until densification.

2.3. Specimens

In the current work, TPMS are used to create architected cellular materials. The methodology adopted to create the computer-aided design (CAD) files of such structures are detailed in the previous works of the authors [32,40]. Cubic TPMS-CM specimens were fabricated

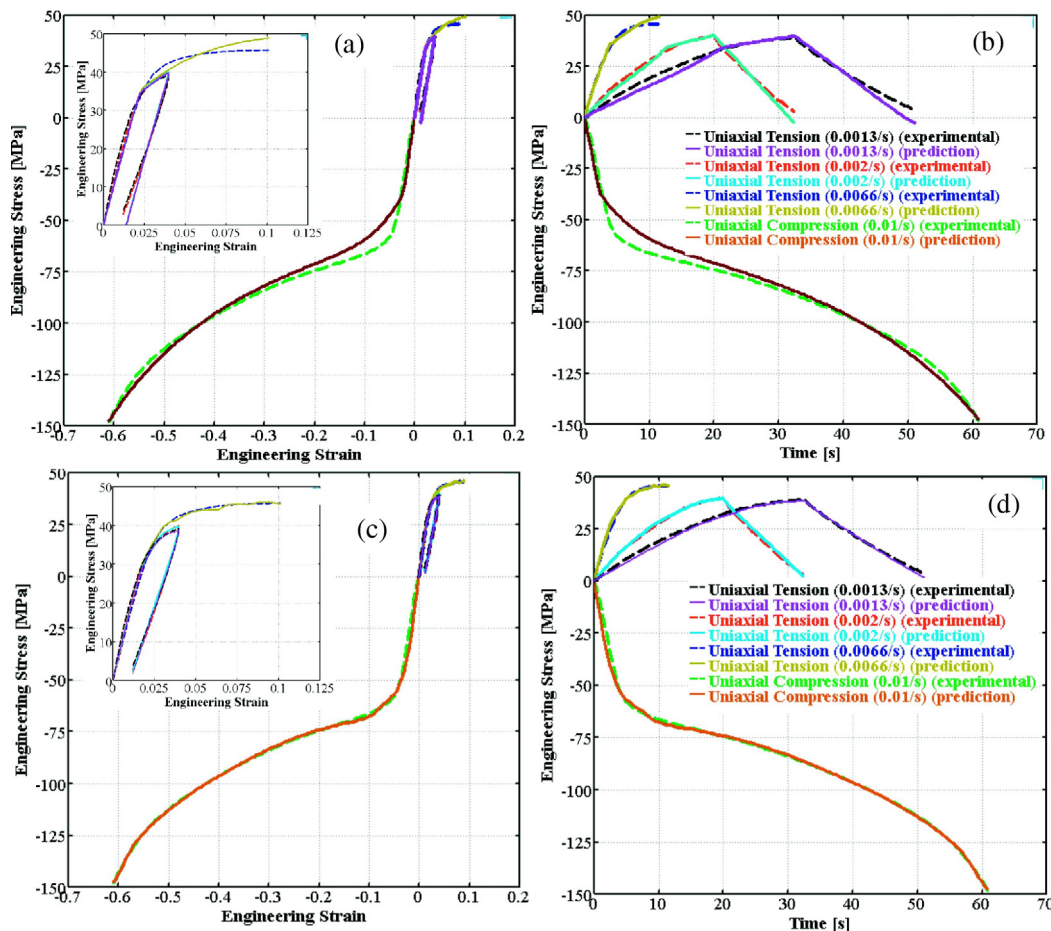


Fig. 4. Description and calibration of constitutive models used. Rheological representation of (a) AB model (b) FEN model. (c) and (d) show the calibration of AB model while (e) and (f) show the calibration of FEN model.

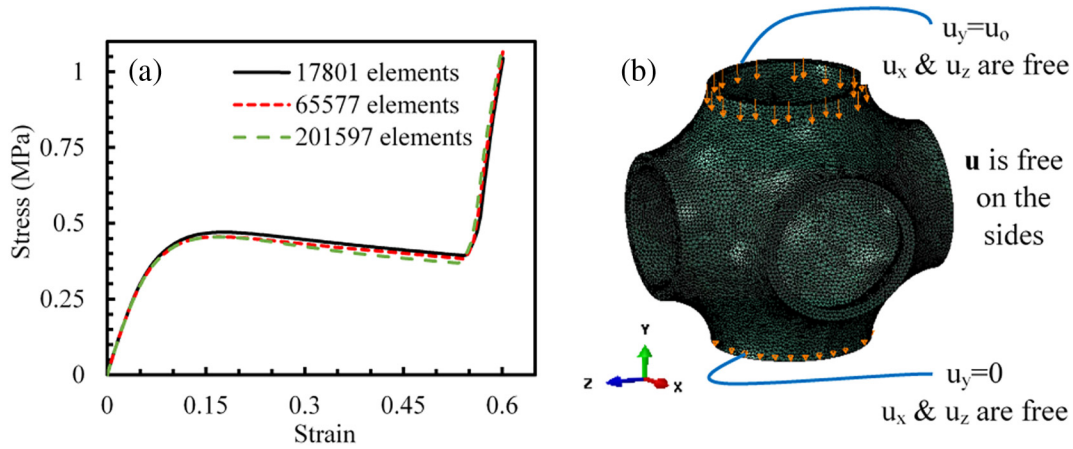


Fig. 5. (a) Mesh sensitivity study performed for Primitive-CM at a relative density of 10%. The results reported in this figure are for 1 (1x1x1). (b) Example of used meshes (201,597 elements) and illustration for mixed boundary condition.

with several relative densities. The dimensions of the specimens were controlled by the resolution of the 3D printer which is determined by the size of the particles (see Fig. 2). The side length of one unit cell was 1.5 cm, and the sizes of specimens (total edge length) were varied to study the effect of scale and boundary conditions on the mechanical response. To produce TPMS-CMs with different relative densities, the thicknesses of the TPMS-CMs were varied. The range of thicknesses for each TPMS-CM is different as TPMS have different surface areas. The thickness of the Primitive-CM has a range spanning from 0.135 mm to 1.6 mm, the IWP-CM has a thickness varying between 0.1 mm and 1.1 mm, and the thickness of the Neovius-CM approximately varies between 0.1 mm and 1 mm. Table 1 shows the relative densities for the different TPMS-CMs considered in this study. Detailed information about the variation of the thickness with the desired relative density is reported in Dalaq et al. [5]. Fig. 1 shows three specimens for the different TPMS-CMs under consideration where each specimen has 1000 unit cells (10x10x10) repeated periodically in 3D.

3. Finite element analysis and constitutive models

The mechanical responses of the three TPMS-CMs were also studied using a finite element method. The analyses were performed using the

software *Abaqus* [53], with large deformation theory of continuum mechanics. The stress-strain behavior of PA 2200 was represented by two constitutive models: Arruda-Boyce (AB) model and flow evolution network (FEN) model which are available in the *PolyUMod* software [48]. The AB model captures an initial linear elastic behavior while the adopted FEN model includes an initial hyperelastic behavior. Both models account for yielding, with yield point being dependent on applied strain rate, and viscoplastic deformation. Fig. 3a and b provide rheological representations for both models to give readers an insight into the models used in the study [47,54]. In fact, AB model and FEN model are three-dimensional models; hence, a tensor acts on each component shown in Fig. 3a and b rather than a scalar. Both models are based on the multiplicative decomposition of the deformation gradient into elastic/hyperelastic and viscoplastic components.

The AB model consists of two networks in series: linear elastic network and viscoplastic network denoted in Fig. 3a by E and P, respectively. The spring in the plastic network represents the back stress Langevin spring which is based on nonlinear hyperelasticity to account for an entropic resistance to chain alignment while the dashpot represents the viscoplastic element which accounts for strain rate dependent yield that monitors an isotropic resistance to chain segment rotation [47, 54]. The FEN model is a versatile constitutive model that can capture

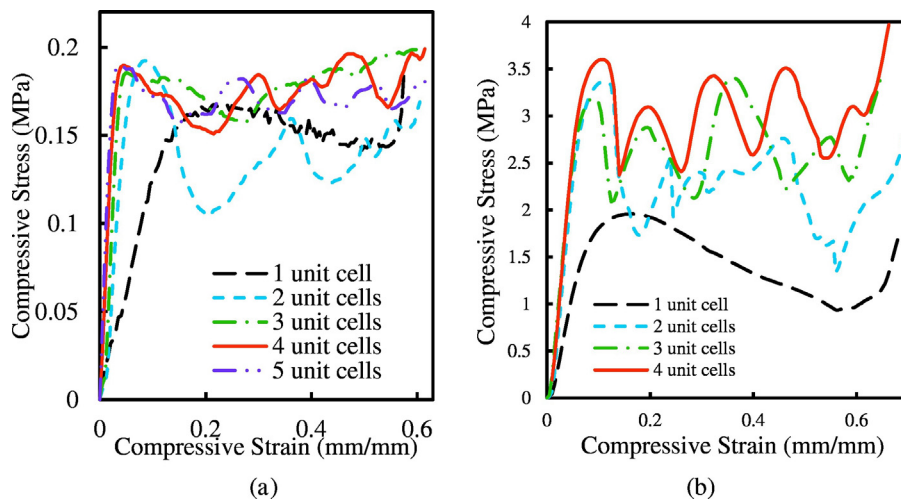


Fig. 6. Effect of specimen size on the mechanical response of the Primitive-CM at a strain rate of 0.01 s^{-1} : (a) relative density of 4%, (b) relative density of 22%. Number of unit cells indicated in the legend represents the number of unit cells in each direction; for example, 3 unit cells corresponds to a total of 27 (3x3x3) unit cells.

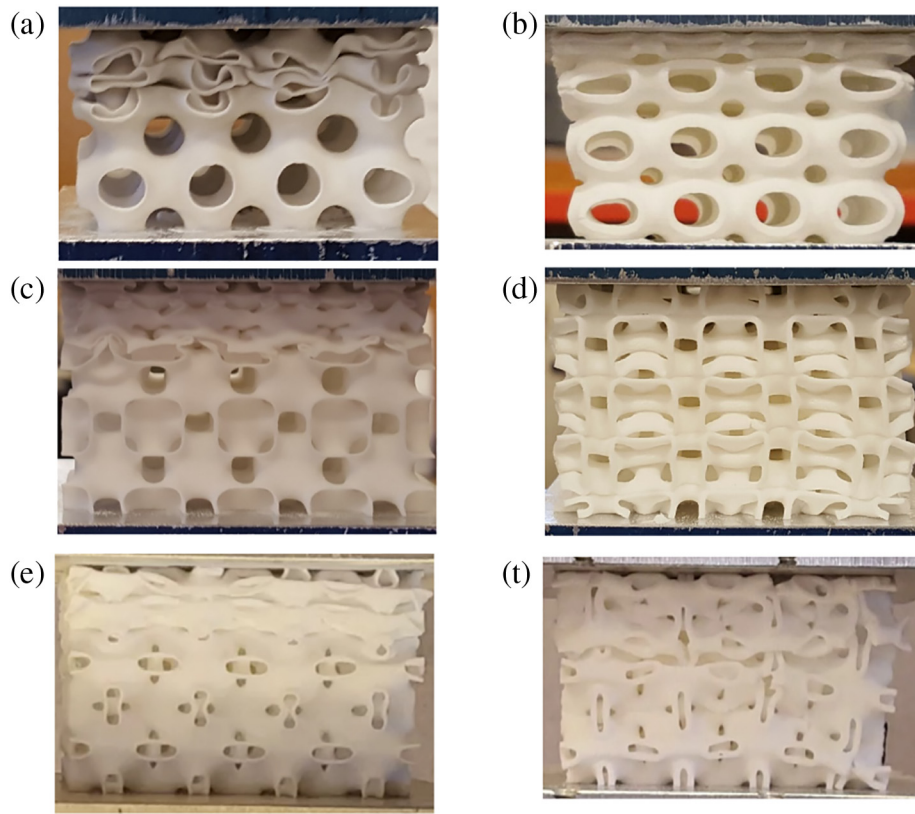


Fig. 7. Deformed specimens: Primitive-CM IWP-CM at a relative density of (a) 4% (b) 24%, IWP-CM at a relative density of (c) 8% (d) 24%, Neovius-CM at a relative density of (e) 10% (f) 24%.

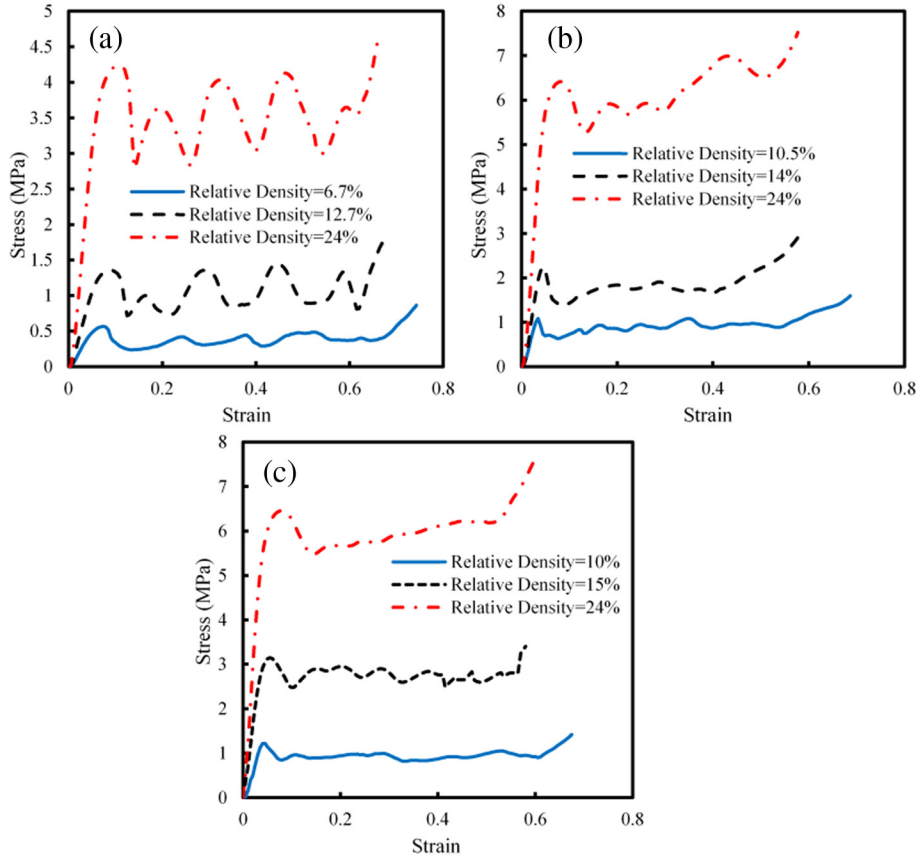


Fig. 8. Example of the variation of the stress-strain curve with the variation of the relative density. The testing was performed for the TPMS-CM with 64 (4x4x4) unit cells at a strain rate of 0.01 s^{-1} (a) Primitive-CM (b) IWP-CM and (c) Neovius-CM.

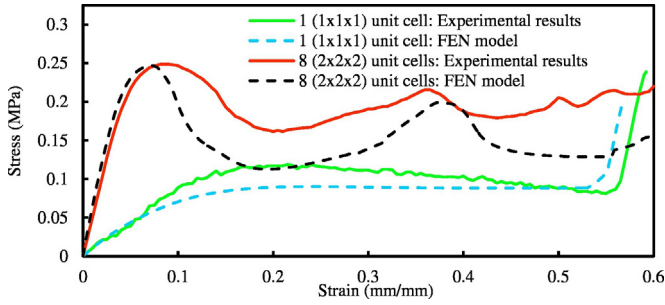


Fig. 9. Comparison between the stress-strain curves of the Primitive-CM at a relative density of 4.5% obtained experimentally and computationally. The applied strain rate is 0.01 s⁻¹.

the mechanical behavior of various polymers [54]. The adopted FEN model consists of four parallel networks (see Fig. 3b) that possess the same constitutive elements, but the material properties are different. Each network consists of a hyperelastic component based on the Holzapfel-Gasser-Ogden anisotropic hyperelastic model [55] (represented by a spring in Fig. 3b) and a viscoplastic component (represented by a dashpot in Fig. 3b) [54,56]. The strain energy density for each network ($i \in [1,4]$) is given by:

$$\Psi_i = f_i p_i \left\{ \Psi_{yi} + \frac{k_1}{2k_2} \sum_{j=1}^3 \left[e^{k_2 R(E_{ji})} - 1 \right] \right\} + f_i \frac{\kappa}{2} (J_i^e - 1)^2, \quad (1)$$

where f_i is a stiffness factor specifying how much stiffer network i is compared to network 1, $J_i^e = \det[\mathbf{F}_i^e]$, $\mathbf{b}_i^e = (J_i^e)^{-2/3} \mathbf{F}_i^e \mathbf{F}_i^{eT}$, $I_{4ji}^e = \text{tr}[\mathbf{b}_i^e]$, and the strain energy Ψ_{yi} is given by the Yeoh model:

$$\Psi_{yi} = C_{10} (I_{1i}^e - 3) + C_{20} (I_{1i}^e - 3)^2 + C_{30} (I_{1i}^e - 3)^3, \quad (2)$$

where $[C_{10}, C_{20}, C_{30}]$ are material parameters, and $I_{1i}^e = \text{tr}[\mathbf{b}_i^e]$ is the first invariant of the elastic left Cauchy-Green tensor. The $[k_1, k_2]$ specifies the anisotropic stiffness factors, and κ is the bulk modulus. The dispersion factors are given by $E_{ji} = d(I_{1i}^e - 3) + (1 - 3d)[I_{4ji}^e - 1]$, $I_{4ji}^e = (\mathbf{F}_i^e \mathbf{a}_j) \cdot (\mathbf{F}_i^e \mathbf{a}_j)$, and $R(x) = (x + |x|)/2$ is the ramp function. The initial orientation directions are taken here to be aligned with the global coordinate system ($\mathbf{a}_i = \mathbf{e}_i$). The elastic stiffness of each network is evolving with the plastic strain to capture material damage:

$$\frac{dp_i}{dt} = \frac{1}{c_e} (f_{ss} - f_{ie^p}) \dot{\gamma}_i^v, \quad (3)$$

where f_{ss} and c_e are material parameters, and the damage state p_i is 0 at time = 0. The total Cauchy stress is given by the sum of the Cauchy stresses in each network.

The viscoplastic flow rate of each network ($i \in [1,4]$) is given by:

$$\dot{\mathbf{F}}_i^v = \dot{\gamma}_i^v \cdot (\mathbf{F}_i^e)^{-1} \frac{\text{dev}[\boldsymbol{\sigma}_i]}{\tau_i} \mathbf{F}_i, \quad (4)$$

$$\dot{\gamma}_i^v = \dot{\gamma}_0 \cdot (\lambda_i^v - 1 + \xi)^C \cdot R \left(\frac{\tau_i}{g h_{i2} h_{i2} \hat{\tau}_i} - \tau_{cut} \right)^m, \quad (5)$$

where $\dot{\gamma}_0 \equiv 1/s$, $\mathbf{b}_i^v = \mathbf{F}_i^v \mathbf{F}_i^{vT}$, $\lambda_i^v = (\text{tr}[\mathbf{b}_i^v]/3)^{1/2}$, $g = R(1 + \frac{p}{p_0})$ where p is the pressure and p_0 is a material parameter controlling the pressure dependence of the flow, and τ_i is the Mises stress from the total stress $\boldsymbol{\sigma}_i$ acting on network i . The flow resistance of the material is evolving with plastic strain following the hardening equations:

$$\frac{dh_{i1}}{dt} = \frac{1}{D_{e1}} (h_{ss1} - h_{i1}) \dot{\gamma}_i^v, \quad (6)$$

$$\frac{dh_{i2}}{dt} = \frac{1}{D_{e2}} (h_{ss2} - h_{i2}) \dot{\gamma}_i^v, \quad (7)$$

where $h_{i1} = h_{i2} = 1$ at time = 0, and $[h_{ss1}, h_{ss2}, D_{e1}, D_{e2}]$ are material parameters. Detailed constitutive relationships for both AB and FEN models can be found in [47,54,56].

The material PA 2200 was tested under different testing modes and strain rates. They include three methods: (1) until failure under tensile load at an engineering strain rate of 0.0066 s⁻¹, (2) tensile loading and unloading at two strain rates (0.002 s⁻¹ and 0.0013 s⁻¹), and under compressive loading until densification at a strain rate of 0.01 s⁻¹. Fig. 4 depicts calibrations of the two models. These strain rates were chosen so the mechanical testing can be considered quasi-static. By observing Fig. 4, one can conclude that both models capture the mechanical response of PA 2200. However, the FEN model has a better agreement with the results obtained experimentally than the AB model.

4. Results and discussion

This section discusses the mechanical behavior of the TPMS-CMs. The finite element analyses were performed using 10-node quadratic tetrahedron (C3D10 from Abaqus library) elements. A mesh sensitivity study was performed for the different TPMS-CMs for all relative densities to ensure objective results. Fig. 5a illustrates an example of the mesh sensitivity study performed: the stress-strain curves of 1 (1x1x1) unit cell of Primitive-CM at a relative density of 10%. This

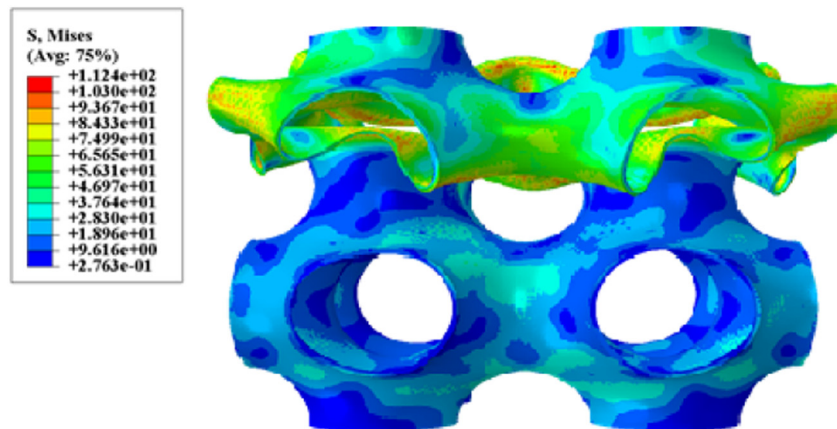


Fig. 10. Primitive-CM with 8 (2x2x2) unit cells deformed under mixed boundary conditions. The Primitive-CM has a relative density of 4.5%, and the applied strain is 20%. The unit of the stress values is kPa, and the deformation scale factor is one.

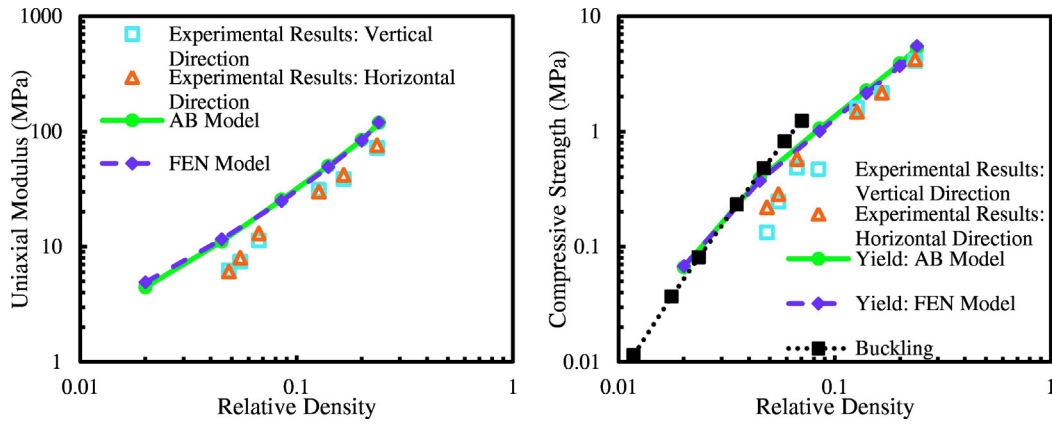


Fig. 11. Compressive uniaxial modulus and strength of Primitive-CM at a strain rate 0.01 s^{-1} . The experimental results are obtained from TPMS-CMs with 64 (4x4) unit cells.

example shows that the analysis is insensitive to the mesh size of the mesh choices used. Fig. 5b illustrates the mixed boundary conditions and an example of meshes used in the mesh sensitivity study. For TPMS-CMs with a larger number of cells, the boundary conditions shown in Fig. 5b are applied on the outer faces of the entire structure rather than the faces of every unit cell. The effect of specimen size on the mechanical response of the TPMS-CMs is investigated to ensure that the results represent the effective response. Fig. 6 shows the effect of specimen size (number of unit cells) on the mechanical response of the Primitive-CM at two relative densities, 4% and 22%. In the elastic region, the deformation is homogeneous, and beyond it, the deformation starts to localize. At a relative density of 4%, when the number of unit cells is changed the mechanical response varies significantly for a low number of unit cells while the variation is small for a higher number of unit cells. For instance, the difference between the strengths in the case of one unit cell and two unit cells is around 15% while the difference between the strengths in the case of four unit cells and five unit cells is approximately 0.01%. Interestingly, one can notice that the number of humps appearing in the stress-strain curves presented in Fig. 6a is the same as the number of unit cells in one direction. This observed behavior is related to how the specimens are deformed. At a relative density of 4%, it is seen that the specimens are collapsing in a layer-by-layer fashion, and each hump represents the collapse of one layer (see Fig. 7a). Moreover, one can conclude that the stress amplitudes and strain spans of the humps appearing in the stress-strain curves decrease when the number of unit cells is increased. Although it is noticed that the deformation is more uniform

when the relative density of the Primitive-CM increases, the deformation of the Primitive-CM is still considered a layer-by-layer collapse (see Fig. 7b). Hence, humps are expected in the stress-strain curves of the Primitive-CM even at high relative densities as shown in Figs. 6 and 8. Similar to the Primitive-CM, a layer-by-layer collapse of the IWP-CM and Neovius-CM at low relative density is noticed, and the specimens fail progressively from specimen boundaries (see Fig. 7c and e). Unlike the Primitive-CM, it is observed that the deformations of the IWP-CM and Neovius at high relative density are spread more uniformly over the specimen with a slight concentration at the center of the specimen (see Fig. 7d and f). Hence, the humps shown in the response of the IWP-CM and Neovius-CM have lower amplitudes compared to the Primitive-CM (see Fig. 8).

Fig. 8 portrays the variation of the stress-strain curve of TPMS-CMs with the relative density. The stress-strain curves start with a linear elastic response followed by a nonlinear stress increase with the strain increase until it reaches the strength of the CM where softening behavior starts. After softening, at small relative densities a plateau-like response is observed; in other words, the hardening slope is approximately zero. In contrast, for large relative densities (e.g. 24%), a low-value positive hardening slope is seen after softening. The plateau-like behavior and low-value hardening slope behavior are due to different mechanisms depending on the properties of the base materials. For elastomeric base material, the governing mechanism is buckling while the governing mechanism for brittle materials (e.g. ceramics) is fracture. For the ductile materials (e.g. metals and some thermoplastics (PA 2200)), the governing mechanism is plastic yielding

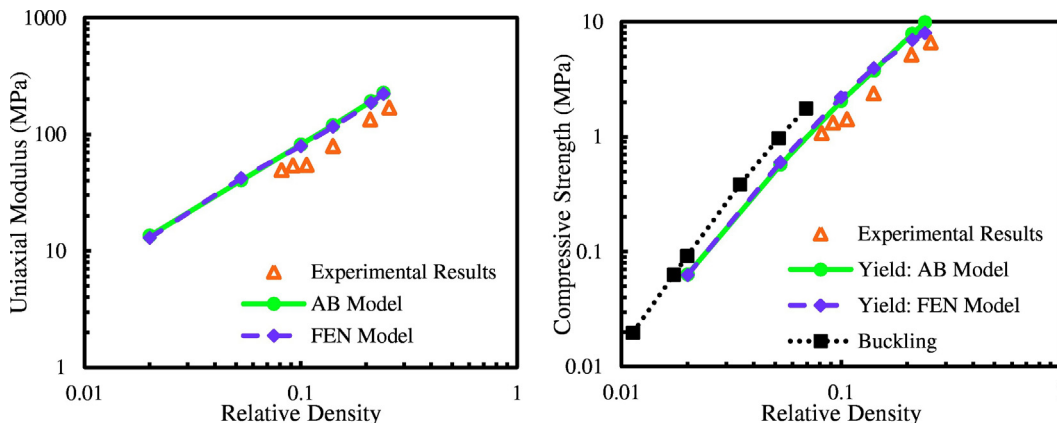


Fig. 12. Compressive uniaxial modulus and strength of IWP-CM at a strain rate 0.01 s^{-1} . The experimental results are obtained from TPMS-CMs with 64 (4x4) unit cells.

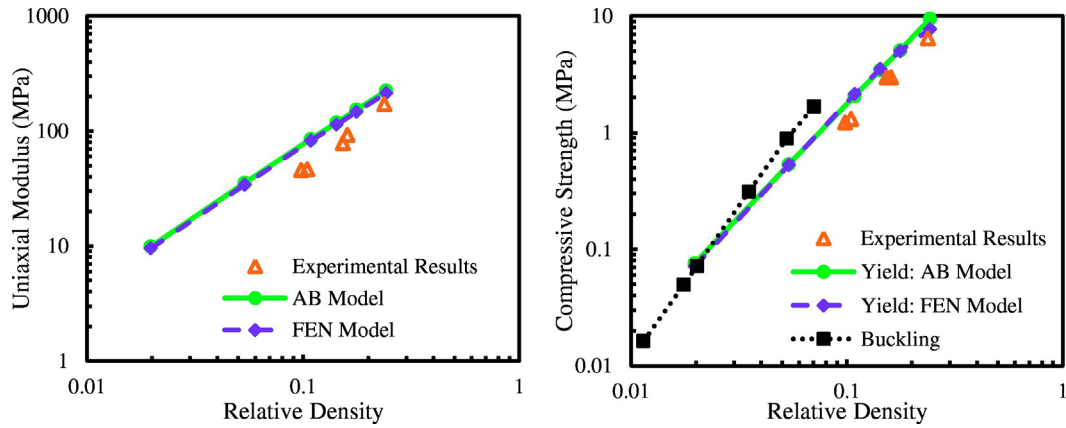


Fig. 13. Compressive uniaxial modulus and strength of Neovius-CM at a strain rate 0.01 s^{-1} . The experimental results are obtained from TPMS-CMs with 64 (4x4) unit cells.

[1]. After that, densification is observed to start. Densification starts at lower strains for CMs with larger relative densities. Fig. 8 shows that the IWP-CM and Neovius-CM have very close results and similar stress-strain curves while the Primitive-CM has a more oscillating behavior with lower compressive modulus and strength compared to the IWP-CM and Neovius-CM. However, the Primitive-CM has higher failure (densification) strains than the other two TPMS-CMs.

Fig. 9 portrays a comparison between the stress-strain curves of the Primitive-CM obtained experimentally and computationally. The Primitive-CM was tested with 1 (1x1x1) unit cell and 8 (2x2x2) unit cells. In the finite element analysis, mixed boundary conditions (mimicking the ones applied in the experiment) are applied. The finite element results are in good agreement with the experimental results. The finite element analysis captures the elastic region, yielding point, and densification region very well. Although there is a discrepancy between the experimental and finite element results in the plateau region, the finite element analysis captures the trend and the humps shown in the experimental curves well. Fig. 10 depicts the stress contours and deformation of the Primitive-CM with 8 (2x2x2) unit cells under mixed boundary conditions. By comparing the deformations in Figs. 7a and 10, one can conclude that the finite element analysis captures the deformation obtained experimentally. It is necessary to distinguish between apparent properties and effective properties. The apparent properties are defined when dealing with finite specimen sizes while the effective properties represent the macroscopic properties [57]. Periodic boundary conditions are used to obtain the effective properties computationally [58,59]. Fig. 11 portrays the variation of the compressive uniaxial modulus and compressive strength of the Primitive-CM with the change of the relative density at an engineering strain rate of 0.01 s^{-1} . Although the uniaxial modulus and strength change with the different printing directions, the difference is relatively small. Selective laser sintering technique produces specimens that are more isotropic than the ones produced by other 3D printing techniques, such as the technique used in work of Dalaq et al. [38], because selective laser sintering is particle-based (see Fig. 2). The effect of printing direction is ignored for simplicity, and only the horizontal direction is investigated. The

material constitutive models are calibrated based on the horizontal direction. Figs. 12 and 13 depict the compressive uniaxial modulus and compressive strength at an applied engineering strain rate of 0.01 s^{-1} for the IWP-CM and Neovius-CM, respectively. The results obtained using the AB model and FEN model are very close to each other and almost coincide.

The relative densities of the 3D printed TPMS-CMs specimens, in general, were deviating from their corresponding CAD files. Such deviations were introduced due to the resolution of the 3D printer and thin walls. The deviation from the CAD was lower when higher relative densities (thicker walls) were considered. Hence, the relative densities used for the experimental results were measured after 3D printing the specimens rather than relying on the relative densities obtained from the CAD files. Furthermore, four specimens were tested for the base material and each relative density of the TPMS-CMs. The mean values are reported in Figs. 11–13. Table 1 summarizes the relative densities of the different TPMS-CMs used in the experimental analyses and their corresponding standard deviations. It was observed that the experimental results are relatively repeatable. The experimental results for the TPMS-CMs can be fitted using a power law equation as presented in Table 2. The TPMS-CMs under a compressive uniaxial loading possess a behavior between the stretching- and bending-dominated modes. The modulus of the IWP-CM has lowest power coefficient with a value of 1.176 which indicates a stretching-dominated behavior. The three TPMS-CM possess close power coefficient values for their compressive strength. It can be seen from Figs. 11–13 that a better agreement between experimental results and computational results using both models is at higher relative densities. The better agreement at higher relative densities (larger thicknesses) is explained by less sensitivity to the printing direction at higher relative densities. Another reason is that fewer defects are observed at higher relative densities; such defects appear due to the limitation of the 3D printer resolution.

Another physical phenomenon that may dictate the compressive strengths of the TPMS-CMs is buckling where structures fail due to loss of their geometric and material stability. As the walls of the TPMS-CMs are much thinner than their overall dimensions, TPMS-CMs can buckle locally under compressive and tensile loads as tensile loading induces local compressive stress as well due to the complex architectures. Bifurcation analysis was performed to estimate the critical buckling loads of the TPMS-CMs. The applied boundary conditions significantly affect the value of the buckling loads. Ultra-light materials tend to locally buckle and/or fracture minimizing the constraining effects from adjacent cells [60,61]. The boundary conditions proposed by Valdevit et al. [60] were used here to determine the local buckling of the TPMS-CMs. In brief, these boundary conditions keep the nodes on the lateral faces to be free while the nodal rotations on the top and

Table 2
Curve fits for the TPMS-CM modulus and strength. ρ , E , and S represent the relative density, compressive uniaxial modulus, and strength, respectively.

TPMS-CM	E (MPa)	S (MPa)
Primitive	$672 (\rho)^{1.518}$	$53 (\rho)^{1.749}$
IWP	$836 (\rho)^{1.176}$	$64 (\rho)^{1.646}$
Neovius	$1669 (\rho)^{1.589}$	$98 (\rho)^{1.886}$

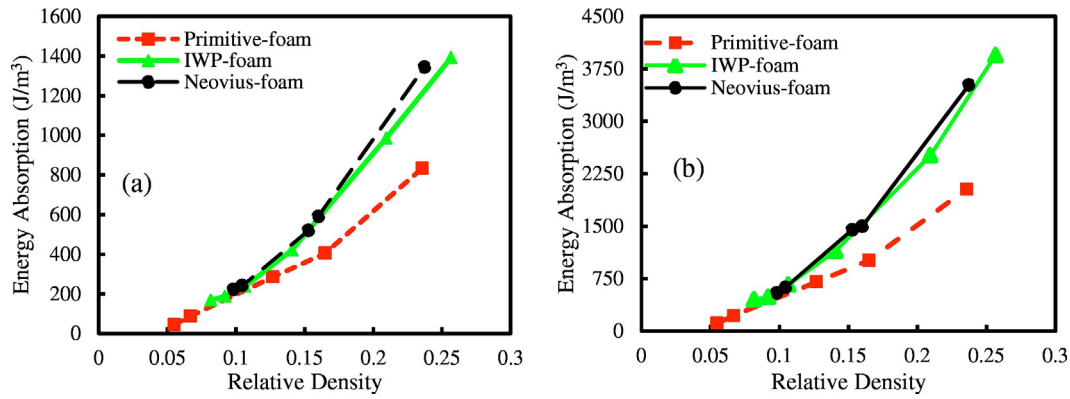


Fig. 14. Energy absorption of TPMS-CMs subjected to a compression of (a) 25% strain (b) 60% strain. The results reported in this figure are obtained experimentally for specimens with size of 64 (4x4x4) unit cells, and the applied strain rate is 0.01 s^{-1} .

bottom faces are assigned zero values. The bottom face was also subjected to a zero displacement in the normal direction, while the top face was subjected to a compressive force load in the normal direction. The buckling results obtained using these boundary conditions are in agreement with the experimental results found in [45,60]. The critical load P_{cr} is calculated by applying a small preload P followed by an incremental load Q ($P_{cr} = P + \lambda Q$) where P is the preload, Q is the incremental load, and λ is smallest positive eigenvalue that leads to buckling [10,53]. It can be seen, from Figs. 11–13, that the strengths of the TPMS-CMs with thinner walls (low relative density) are governed by buckling while those associated with thicker walls (high relative density) are governed by plastic yielding. More specifically, the elastic buckling-yielding transition occurs approximately at 2.5%, 1%, and 2% for the Primitive-CM, IWP-CM, and Neovius-CM, respectively. Moreover, the experimental study is carried out over the high relative densities region which corresponds to the plastic yield regime for the three TPMS-CMs.

Fig. 14 shows the variation of the energy absorption of the TPMS-CMs with the variation of the relative density. The energy absorption is defined in the current paper as the area under the stress-strain curve under a compressive strain of 25% and 60%. The results reported in Fig. 14 are for specimen size of 64 (4x4x4) unit cells and the applied strain rate of 0.01 s^{-1} . At low relative densities, there is not much difference in the energy absorbed by each geometry. It is observed that Neovius-CM has highest energy absorption while the Primitive-CM has lowest energy absorption. From Figs. 11–14, one concludes that

the performance of the IWP-CM and Neovius-CM are close to each other as shown in Fig. 15 while the Primitive-CM possesses lower uniaxial modulus, strength, and energy absorption compared to the IWP-CM and Neovius-CM. Nonetheless, Abueidda et al. [32] have shown that the shear modulus of the Primitive-CM is higher than the shear-moduli of the IWP-CM and Neovius-CM while the three TPMS-CMs interestingly have almost the same bulk modulus. The similarity in the performance of the Neovius-CM and IWP-CM is justified by the similarity in the geometric properties of the two CMs. Dalaq et al. [5] showed that the IWP-CM and Neovius-CM have similar geometric properties (moment of inertia, surface area, cross-sectional area, and thickness at a certain relative density). Also, the uniaxial moduli and compressive strengths of the TPMS-CMs are located close to the upper boundary of foam when compared with other materials as shown in Figs. 15 and 16. Furthermore, the base material used to fabricate the TPMS-CM is a polymer; hence, using higher strain rates will result in higher uniaxial modulus and strength. Fig. 17 experimentally shows the effect of strain rate on the mechanical response of the TPMS-CMs. Increasing the applied strain rate leads to higher stiffness and strength while the strain at which densification starts decreases with the increase of the applied strain rate. TPMS-CMs were tested at an engineering strain rates of 0.001 s^{-1} , 0.01 s^{-1} , and 0.1 s^{-1} . These certain strain rates were chosen so the compression test can be considered quasi-static [43,62].

Therefore, the TPMS-CMs possess promising results that are competing with other cellular materials. Better properties for the TPMS-

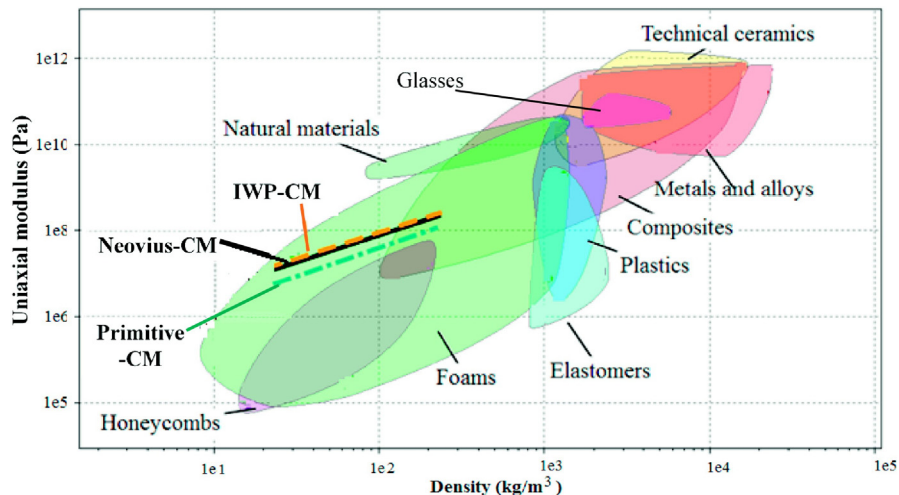


Fig. 15. Comparison between the uniaxial modulus of 3D printed polymeric TPMS-CMs and uniaxial modulus of other materials [1,2,10,64].

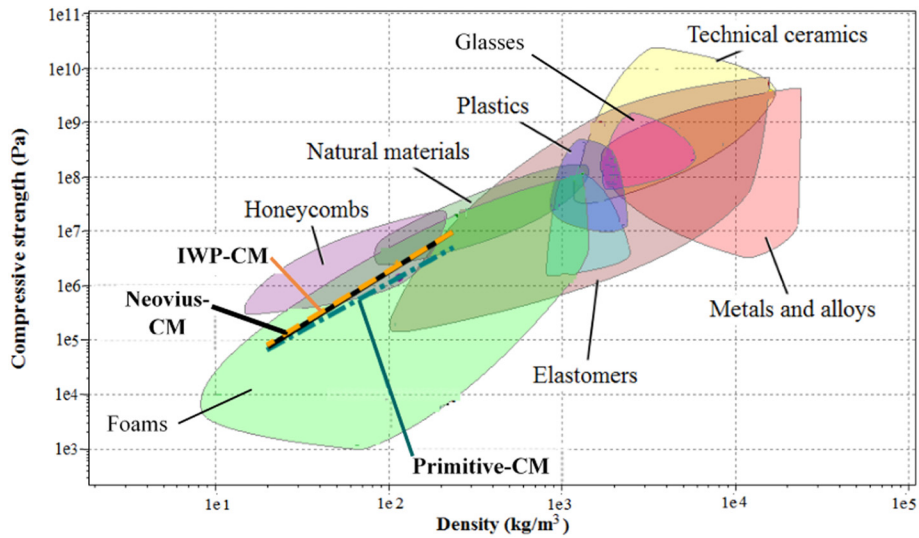


Fig. 16. Comparison between the compressive strength of 3D printed polymeric TPMS-CMs and compressive strength of other materials [1,2,10,64].

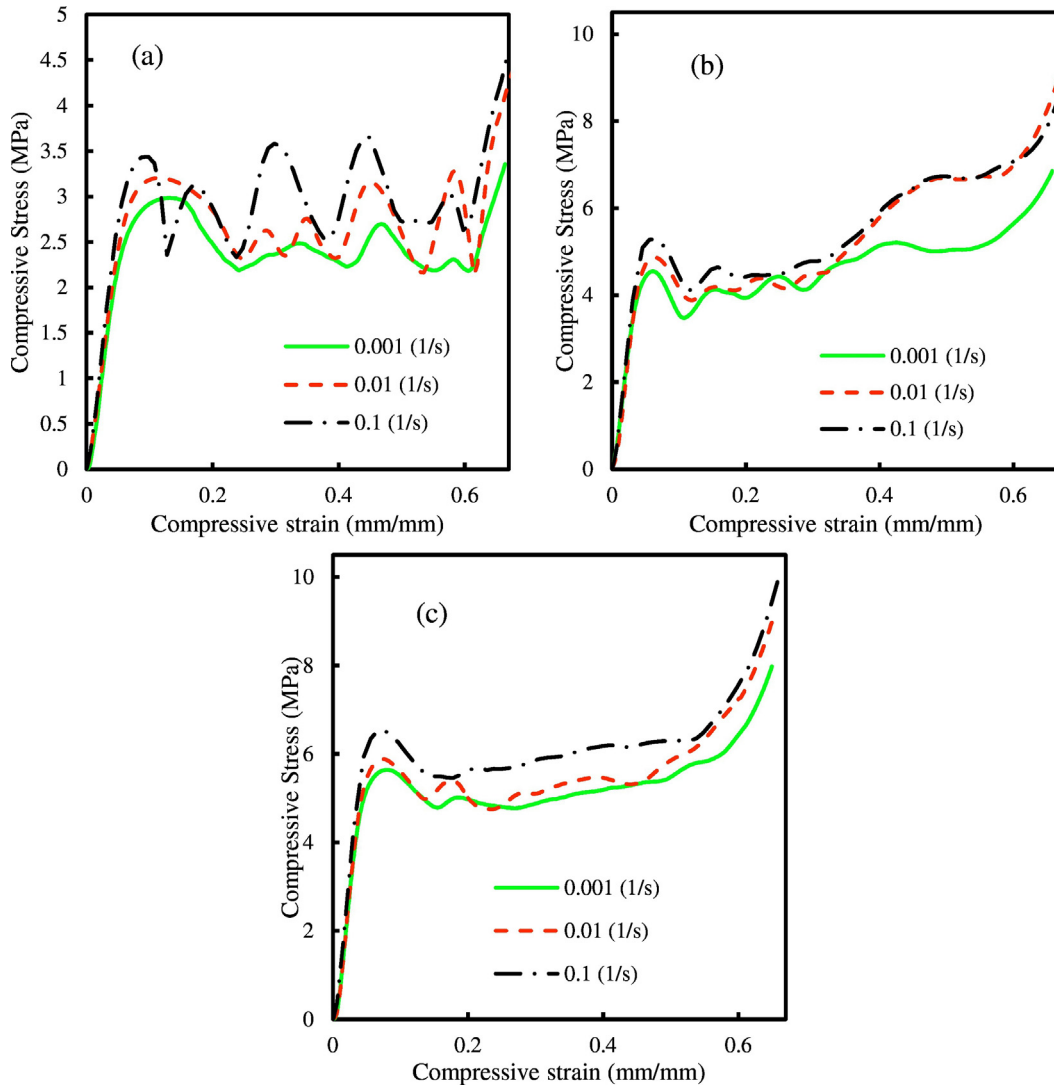


Fig. 17. Effect of applied strain rate on the mechanical response of the TPMS-CMs: (a) Primitive-CM at a relative density of 19.5%, (b) IWP-CM at a relative density of 21%, and (c) Neovius-CM at a relative density of 22%.

CMs are expected if enhanced fabrication techniques and material types (such as ceramics and metals) were utilized [44]. Enhanced properties of the TPMS-CMs can be obtained if TPMS-CMs are fabricated at the micro- or nano-scale using other fabrication techniques such as making a self-propagating photopolymer template followed by metal plating and etching [10,31]. Furthermore, fabrication techniques including atomic layer deposition, metal 3D printing, and other, may lead to structures with promising mechanical properties [30,63].

5. Limitations of the finite element study

Figs. 11–13 show the finite element simulation (based on *Abaqus*) and the experimental results. The calibration of the constitutive model was based on uniaxial tensile and compressive loadings. Such type of testing does not capture some physics (e.g. the effect of Poisson's ratio and hydrostatic loading). Triaxial testing for the base material enhances the quality of calibration, but it was not performed for simplicity. Furthermore, the surface between the load frame and specimens was assumed to be frictionless. Another factor that contributes to the discrepancy between the experimental and computational results is the effect of anisotropy as discussed in the previous sections. Moreover, the variations (e.g. the wall thickness) in the 3D printed specimen plays a role in the discrepancy between the computational and experimental results as stochastic model was not considered in this study. In addition, the TPMS-CMs are fabricated from sintered powdered polymer. Hence, voids are expected within the TPMS-CMs which may cause the structure to buckle at lower loads. The voids are not considered in the finite element analysis.

6. Conclusions

In this paper, 3D cellular materials that are based on mathematical surfaces called triply periodic minimal surfaces (TPMS) were created. Their structures do not possess any joints or discontinuities to minimize the effect of stress concentration. 3D printing was utilized to fabricate the TPMS-CMs. Their mechanical performance was analyzed through a combination of experiments and finite element simulations. The base material was tested under compressive and tensile loadings at different applied strain rates, and the obtained results were used to calibrate the constitutive models employed in the computational analysis. The effects of the applied boundary conditions and size of the specimen were also studied. It is shown that mechanical response of the TPMS-CMs obtained computationally and experimentally are in reasonable agreement. IWP-CM and Neovius-CM have a highest uniaxial compressive modulus, compressive strength, and energy absorption. The TPMS-CMs show superior properties when compared with other cellular structure, and thus are promising candidates for various technological applications.

Acknowledgements

The NSF Center for Novel High Voltage/Temperature Materials and Structures supported this research [NSF I/UCRC (IIP-1362146)]. The findings, conclusions, and recommendations expressed in this manuscript are those of the authors and do not necessarily reflect the views of the NSF.

References

- [1] L.J. Gibson, M.F. Ashby, *Cellular Solids: Structure and Properties*, Cambridge University Press, 1999.
- [2] M.F. Ashby, H.R. Shercliff, D. Cebon, *Materials: Engineering, Science, Processing and Design*, Butterworth-Heinemann, 2013.
- [3] N.A. Fleck, V.S. Deshpande, M.F. Ashby, *Micro-architected materials: past, present and future*, Proceedings of the Royal Society of London A: Mathematical, Physical and Engineering Sciences, The Royal Society 2010, pp. 2495–2516.
- [4] J. Xiong, R. Mines, R. Ghosh, A. Vaziri, L. Ma, A. Ohrndorf, H.J. Christ, L. Wu, *Advanced micro-lattice materials*, *Adv. Eng. Mater.* 17 (9) (2015) 1253–1264.
- [5] A.S. Dalaq, D.W. Abueidda, R.K. Abu Al-Rub, I.M. Jasiuk, *Finite element prediction of effective elastic properties of interpenetrating phase composites with architected 3D sheet reinforcements*, *Int. J. Solids Struct.* 83 (2016) 169–182.
- [6] F.A. Sabet, A. Raiesi Najafi, E. Hamed, I. Jasiuk, *Modelling of bone fracture and strength at different length scales: a review*, *Interface Focus* 6 (1) (2016).
- [7] L. Valdevit, A.J. Jacobsen, J.R. Greer, W.B. Carter, *Protocols for the optimal design of multi-functional cellular structures: from hypersonics to micro-architected materials*, *J. Am. Ceram. Soc.* 94 (s1) (2011).
- [8] L.J. Gibson, *Biomechanics of cellular solids*, *J. Biomech.* 38 (3) (2005) 377–399.
- [9] S. Khaderi, V.S. Deshpande, N.A. Fleck, *The stiffness and strength of the gyroid lattice*, *Int. J. Solids Struct.* 51 (23) (2014) 3866–3877.
- [10] B.D. Nguyen, J.S. Cho, K. Kang, *Optimal design of "Shellular", a micro-architected material with ultralow density*, *Mater. Des.* 95 (2016) 490–500.
- [11] V.S. Deshpande, M.F. Ashby, N.A. Fleck, *Foam topology: bending versus stretching dominated architectures*, *Acta Mater.* 49 (6) (2001) 1035–1040.
- [12] X. Zheng, H. Lee, T.H. Weisgraber, M. Shusteff, J. DeOtte, E.B. Duoss, J.D. Kuntz, M.M. Biener, Q. Ge, J.A. Jackson, S.O. Kucheyev, N.X. Fang, C.M. Spadaccini, *Ultralight, ultrastiff mechanical metamaterials*, *Science* 344 (6190) (2014) 1373–1377.
- [13] J. Bauer, A. Schroer, R. Schwaiger, O. Kraft, *The impact of size and loading direction on the strength of architected lattice materials*, *Adv. Eng. Mater.* 18 (9) (2016) 1537–1543.
- [14] D. Mohr, *Mechanism-based multi-surface plasticity model for ideal truss lattice materials*, *Int. J. Solids Struct.* 42 (11) (2005) 3235–3260.
- [15] A. Vigliotti, V.S. Deshpande, D. Pasini, *Non linear constitutive models for lattice materials*, *J. Mech. Phys. Solids* 64 (2014) 44–60.
- [16] C. Tekoglu, L.J. Gibson, T. Pardo, P.R. Onck, *Size effects in foams: experiments and modeling*, *Prog. Mater. Sci.* 56 (2) (2011) 109–138.
- [17] T.A. Schaedler, W.B. Carter, *Architected cellular materials*, *Annu. Rev. Mater. Res.* 46 (2016) 187–210.
- [18] Q. Zhang, X. Yang, P. Li, G. Huang, S. Feng, C. Shen, B. Han, X. Zhang, F. Jin, F. Xu, T.J. Lu, *Bioinspired engineering of honeycomb structure – using nature to inspire human innovation*, *Prog. Mater. Sci.* 74 (2015) 332–400.
- [19] D. Restrepo, N.D. Mankame, P.D. Zavattieri, *Programmable materials based on periodic cellular solids. Part I: experiments*, *Int. J. Solids Struct.* 100–101 (2016) 485–504.
- [20] K.K. Saxena, R. Das, E.P. Calius, *Three decades of auxetics research – materials with negative Poisson's ratio: a review*, *Adv. Eng. Mater.* 18 (11) (2016) 1847–1870.
- [21] Y. Liu, H. Hu, *A review on auxetic structures and polymeric materials*, *Sci. Res. Essays* 5 (10) (2010) 1052–1063.
- [22] H. Mitschke, J. Schwerdtfeger, F. Schury, M. Stingl, C. Körner, R.F. Singer, V. Robins, K. Mecke, G.E. Schröder-Turk, *Finding auxetic frameworks in periodic tessellations*, *Adv. Mater.* 23 (22–23) (2011) 2669–2674.
- [23] M. Mir, M.N. Ali, J. Sami, U. Ansari, *Review of mechanics and applications of auxetic structures*, *Adv. Mater. Sci. Eng.* 2014 (2014).
- [24] K. Bertoldi, P.M. Reis, S. Willshaw, T. Mullin, *Negative Poisson's ratio behavior induced by an elastic instability*, *Adv. Mater.* 22 (3) (2010) 361–366.
- [25] S. Iio, K. Hasegawa, S. Fushimi, A. Yonezu, X. Chen, *On compressive deformation behavior of hollow-strut cellular materials*, *Mater. Des.* 105 (2016) 1–8.
- [26] M. Bakir, J.L. Meyer, J. Economy, I. Jasiuk, *Heat-induced polycondensation reaction with self-generated blowing agent forming aromatic thermosetting copolyester foams*, *Macromolecules* 49 (17) (2016) 6489–6496.
- [27] K. Taki, T. Yanagimoto, E. Funami, M. Okamoto, M. Ohshima, *Visual observation of CO₂ foaming of polypropylene-clay nanocomposites*, *Polym. Eng. Sci.* 44 (6) (2004) 1004–1011.
- [28] Q. Li, L.M. Matuana, *Foam extrusion of high density polyethylene/wood-flour composites using chemical foaming agents*, *J. Appl. Polym. Sci.* 88 (14) (2003) 3139–3150.
- [29] A.K. Bledzki, O. Faruk, *Microcellular injection molded wood fiber-PP composites: part I - effect of chemical foaming agent content on cell morphology and physico-mechanical properties*, *J. Cell. Plast.* 42 (1) (2006) 63–76.
- [30] T. Tanchogne-Dejean, A.B. Spierings, D. Mohr, *Additively-manufactured metallic micro-lattice materials for high specific energy absorption under static and dynamic loading*, *Acta Mater.* 116 (2016) 14–28.
- [31] T.A. Schaedler, A.J. Jacobsen, A. Torrents, A.E. Sorensen, J. Lian, J.R. Greer, L. Valdevit, W.B. Carter, *Ultralight metallic microlattices*, *Science* 334 (6058) (2011) 962–965.
- [32] D.W. Abueidda, R.K. Abu Al-Rub, A.S. Dalaq, D.-W. Lee, K.A. Khan, I.M. Jasiuk, *Effective conductivities and elastic moduli of novel foams with triply periodic minimal surfaces*, *Mech. Mater.* 95 (2016) 102–115.
- [33] M. Afshar, A.P. Anaraki, H. Montazerian, J. Kadkhodapour, *Additive manufacturing and mechanical characterization of graded porosity scaffolds designed based on triply periodic minimal surface architectures*, *J. Mech. Behav. Biomed. Mater.* 62 (2016) 481–494.
- [34] S.C. Kapfer, S.T. Hyde, K. Mecke, C.H. Arns, G.E. Schröder-Turk, *Minimal surface scaffold designs for tissue engineering*, *Biomaterials* 32 (29) (2011) 6875–6882.
- [35] S.-D. Yang, H.G. Lee, J. Kim, *A phase-field approach for minimizing the area of triply periodic surfaces with volume constraint*, *Comput. Phys. Commun.* 181 (6) (2010) 1037–1046.
- [36] H.-Y. Chen, Y. Kwon, K. Thornton, *Multifunctionality of three-dimensional self-assembled composite structure*, *Scr. Mater.* 61 (1) (2009) 52–55.
- [37] Y. Jung, S. Torquato, *Fluid permeabilities of triply periodic minimal surfaces*, *Phys. Rev. E* 72 (5) (2005) 056319.
- [38] A.S. Dalaq, D.W. Abueidda, R.K. Abu Al-Rub, *Mechanical properties of 3D printed interpenetrating phase composites with novel architected 3D solid-sheet reinforcements*, *Compos. A: Appl. Sci. Manuf.* 84 (2016) 266–280.
- [39] R.K. Abu Al-Rub, D.W. Abueidda, A.S. Dalaq, *Thermo-electro-mechanical properties of interpenetrating phase composites with periodic architected reinforcements*,

- From Creep Damage Mechanics to Homogenization Methods, Springer International Publishing 2015, pp. 1–18.
- [40] D.W. Abueidda, A.S. Dalaq, R.K. Abu Al-Rub, H.A. Younes, Finite element predictions of effective multifunctional properties of interpenetrating phase composites with novel triply periodic solid shell architected reinforcements, *Int. J. Mech. Sci.* 92 (2015) 80–89.
- [41] D.W. Abueidda, A.S. Dalaq, R.K. Abu Al-Rub, I. Jasiuk, Micromechanical finite element predictions of a reduced coefficient of thermal expansion for 3D periodic architected interpenetrating phase composites, *Compos. Struct.* 133 (2015) 85–97.
- [42] D.W. Abueidda, R.K. Abu Al-Rub, A.S. Dalaq, H.A. Younes, A.A. Al Ghaferi, T.K. Shah, Electrical conductivity of 3D periodic architected interpenetrating phase composites with carbon nanostructured-epoxy reinforcements, *Compos. Sci. Technol.* 118 (2015) 127–134.
- [43] L. Wang, J. Lau, E.L. Thomas, M.C. Boyce, Co-continuous composite materials for stiffness, strength, and energy dissipation, *Adv. Mater.* 23 (13) (2011) 1524–1529.
- [44] S.C. Han, J.W. Lee, K. Kang, A new type of low density material: shellular, *Adv. Mater.* 27 (37) (2015) 5506–5511.
- [45] M.G. Lee, J.W. Lee, S.C. Han, K. Kang, Mechanical analyses of “Shellular”, an ultralow-density material, *Acta Mater.* 103 (2016) 595–607.
- [46] E.M. Arruda, M.C. Boyce, R. Jayachandran, Effects of strain rate, temperature and thermomechanical coupling on the finite strain deformation of glassy polymers, *Mech. Mater.* 19 (2) (1995) 193–212.
- [47] E.M. Arruda, M.C. Boyce, Evolution of plastic anisotropy in amorphous polymers during finite straining, *Int. J. Plast.* 9 (6) (1993) 697–720.
- [48] J. Bergström, PolyUMod User’s Manual, Veryst Engineering, LLC, Needham, MA, 2009.
- [49] M. Elhebeary, M.T.A. Saif, Design, simulation, and testing of a novel bending stage for mechanical characterization of materials, *Exp. Mech.* 57 (1) (2017) 89–96.
- [50] J.A. Coy, C.-M. Kuball, D.B. Roppenecker, T.C. Lueth, Flexural modulus of lasersintered PA 2200, ASME 2013 International Mechanical Engineering Congress and Exposition, American Society of Mechanical Engineers, San Diego, USA, 2013 (p. V02AT02A011).
- [51] N. Lammens, M. Kersemans, I. De Baere, W. Van Paepegem, On the visco-elastoplastic response of additively manufactured polyamide-12 (PA-12) through selective laser sintering, *Polym. Test.* 57 (2017) 149–155.
- [52] W. Cooke, R. Anne Tomlinson, R. Burguete, D. Johns, G. Vanard, Anisotropy, homogeneity and ageing in an SLS polymer, *Rapid Prototyp. J.* 17 (4) (2011) 269–279.
- [53] Abaqus, ABAQUS Documentation, Dassault Systèmes, 2012.
- [54] J. Bergström, 8 - viscoplasticity models, *Mechanics of Solid Polymers*, William Andrew Publishing 2015, pp. 371–436.
- [55] G.A. Holzapfel, T.C. Gasser, R.W. Ogden, A new constitutive framework for arterial wall mechanics and a comparative study of material models, *J. Elast. Phys. Sci. Solid* 61 (1–3) (2000) 1–48.
- [56] E.M. Arruda, M.C. Boyce, A three-dimensional constitutive model for the large stretch behavior of rubber elastic materials, *J. Mech. Phys. Solid* 41 (2) (1993) 389–412.
- [57] M. Jiang, K. Alzebedeh, I. Jasiuk, M. Ostoja-Starzewski, Scale and boundary conditions effects in elastic properties of random composites, *Acta Mech.* 148 (1–4) (2001) 63–78.
- [58] S. Li, Boundary conditions for unit cells from periodic microstructures and their implications, *Compos. Sci. Technol.* 68 (9) (2008) 1962–1974.
- [59] M. Jiang, I. Jasiuk, M. Ostoja-Starzewski, Apparent thermal conductivity of periodic two-dimensional composites, *Comput. Mater. Sci.* 25 (3) (2002) 329–338.
- [60] L. Valdevit, S.W. Godfrey, T.A. Schaedler, A.J. Jacobsen, W.B. Carter, Compressive strength of hollow microlattices: experimental characterization, modeling, and optimal design, *J. Mater. Res.* 28 (17) (2013) 2461–2473.
- [61] A. Torrents, T. Schaedler, A. Jacobsen, W. Carter, L. Valdevit, Characterization of nickel-based microlattice materials with structural hierarchy from the nanometer to the millimeter scale, *Acta Mater.* 60 (8) (2012) 3511–3523.
- [62] M.C. Saha, H. Mahfuz, U.K. Chakravarty, M. Uddin, M.E. Kabir, S. Jeelani, Effect of density, microstructure, and strain rate on compression behavior of polymeric foams, *Mater. Sci. Eng. A* 406 (1–2) (2005) 328–336.
- [63] L.R. Meza, J.R. Greer, Mechanical characterization of hollow ceramic nanolattices, *J. Mater. Sci.* 49 (6) (2013) 2496–2508.
- [64] M.F. Ashby, The properties of foams and lattices, *Philos. Trans. R. Soc. London A Math. Phys. Eng. Sci.* 364 (1838) (2006) 15–30.